

Detection of a zero-energy bound state induced on high-temperature superconductor one-unit-cell FeSe/SrTiO₃

Chaofei Liu¹, Ziqiao Wang¹, Cheng Chen¹, Yi Liu¹, Shusen Ye¹, Jiangping Hu^{2,3,4,5}, Jian Wang^{1,4,5}†

¹International Center for Quantum Materials, School of Physics, Peking University, Beijing 100871, China

²Beijing National Laboratory for Condensed Matter Physics & Institute of Physics, Chinese Academy of Sciences, Beijing 100190, China

³Kavli Institute of Theoretical Sciences, University of Chinese Academy of Sciences, Beijing 100190, China

⁴Collaborative Innovation Center of Quantum Matter, Beijing, China

⁵CAS Center for Excellence in Topological Quantum Computation, University of Chinese Academy of Sciences, Beijing 100190, China

†Corresponding author. E-mail: jianwangphysics@pku.edu.cn

Majorana zero modes (MZMs) that obey the non-Abelian statistics have been intensively investigated for potential applications in topological quantum computing. The prevailing signal in tunneling experiments “fingerprinting” the existence of MZM is the zero-energy bound state (ZEBS). However, nearly all of the previously reported ZEBSs showing signatures of the MZMs are observed in difficult-to-fabricate heterostructures and survived at very low temperatures. By using *in situ* scanning tunneling spectroscopy, we detect a ZEBS upon Fe adatom on one-unit-cell FeSe/SrTiO₃(001) that exhibits the highest transition temperature among iron-based superconductors. The experimental findings are partially consistent with the spectroscopic characteristics of the MZM, which may stimulate future MZM explorations in connate topological superconductors and towards an applicable temperature regime.

Quasiparticle excitations in superconductors are substantially dependent of the impurity-scattering potentials, Cooper pairing symmetry (1) and Andreev-reflection processes (2), etc. The zero-energy bound state (ZEBS) among them is particularly noteworthy, which possibly originates from the topologically nontrivial Majorana zero mode (MZM) (3). Obeying the non-Abelian braiding statistics, the MZM is a potential building block for the fault-tolerant quantum computation (4). Recently prevailing MZM platforms include semiconducting nanowires (NWs) (5), Fe atomic chains (6) and topological-insulator ultrathin films (7) in proximity to Bardeen-Cooper-Schrieffer (BCS) superconductors. These implementations have detected the theoretically predicted ZEBSs in the presence of MZMs (8-11). However, the heterostructure-fabricating difficulty and low experimental temperature (primarily ≤ 1.4 K) for those designs make future applications in quantum-functionality electronics highly challenging.

The high-temperature superconducting (SC) iron chalcogenides specify alternative directions for pursuing the MZMs (12-15). For example, the simultaneously discovered Dirac-type spin-helical surface state and an induced *s*-wave SC gap in a single iron-chalcogenide material, FeTe_{0.55}Se_{0.45}, highlight the existence of connate high-temperature topological superconductivity (16). Consistently, the ZEBSs bearing the characteristics of MZMs in topological superconducting (TSC) states have been observed in interstitial iron impurities (IFIs) and magnetic vortices of Fe(Te,Se) single crystals (17, 18). Although Fe(Te,Se) is a nominally perceived high-temperature superconductor, its SC transition temperature (T_c) is generically limited below 15 K (17). The relatively low T_c of Fe(Te,Se), together with the difficult-to-control character of induced magnetic vortices therein, poses barriers to technically realizing and freely manipulating the MZMs. One-unit-cell (1-UC) FeSe/SrTiO₃(001) (19) (Fig. 1A), showing an extremely high T_c of ~40–109 K (20, 21) and being predicted to be topologically SC (15), exemplifies an ingenious platform to address these issues. Additionally, while the magnetically ordered Yu-Shiba-Rusinov (YSR) (magnetic) chains on BCS superconductors have been systematically investigated to explore the MZMs (6), the individual-YSR-atom-based MZM configurations are scarcely proposed.

Here, we report the ZEBS induced by Fe adatom on 1-UC FeSe/SrTiO₃(001) via *in situ* scanning tunneling

spectroscopy (4.2 K unless specified) (22). The experimental results partially resemble the phenomenological signatures of the MZM, although further decisive studies are still necessary to completely exclude the possibility of zero-energy impurity state. In Brillouin zone (BZ), the Fermi surface of 1-UC FeSe/SrTiO₃(001) only consists of electron pockets at the M points (Fig. 1, B and C) (21). By the molecular-beam epitaxy (MBE) technique (22), our 1-UC FeSe film was well prepared with an atomically flat surface in both mesoscopic and microscopic scales (Fig. 1, D and E). As previous reports (19, 21), the tunneling spectrum (dI/dV vs. V) measured on 1-UC FeSe surface is fully gapped and typified with the multiband superconductivity as suggested by high-resolution photoemission spectroscopy (Fig. 1F) (23). Along the trajectory in a single domain, the spatially resolved spectra repeatedly reveal the multiband pairing state with SC gaps (Δ_1, Δ_2 ; $\Delta_1 < \Delta_2$) near 9.5 and 16.0 meV for Δ_1 and Δ_2 , respectively (Fig. 1G). Therefore, a pristine high-temperature SC substrate [1-UC FeSe/SrTiO₃(001)] for adsorbate (Fe adatom) deposition is well established.

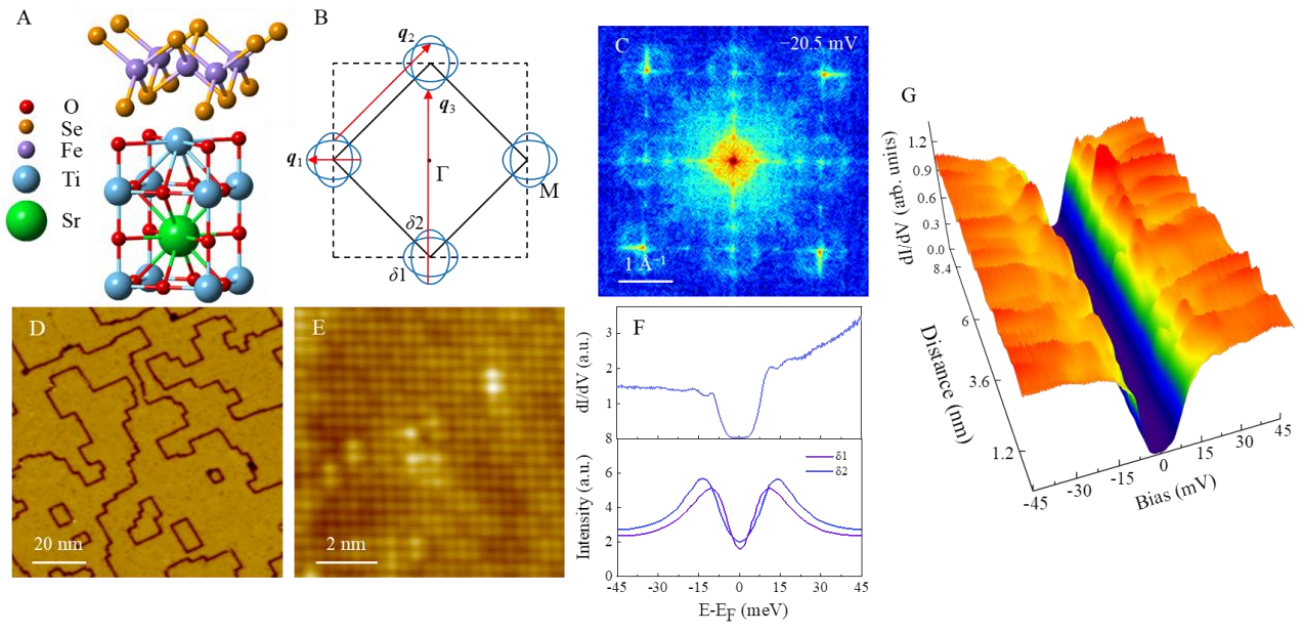


Fig. 1. Crystal structure, topographies and multiband superconductivity of 1-UC FeSe/SrTiO₃(001). (A) Crystal structure and (B) Fermi-surface topology in the folded BZ (solid black square) of 1-UC FeSe/SrTiO₃(001). The unfolded BZ (dashed black square) is shown for comparison. \mathbf{q}_1 , \mathbf{q}_2 and \mathbf{q}_3 : possible scattering vectors. (C) Fast Fourier transformation of the dI/dV mapping at -20.5 mV measured on pristine 1-UC FeSe surface (28×28 nm²; set point: $V = 0.06$ V, $I = 500$ pA; modulation: $V_{\text{mod}} = 1$ mV). Pocket-like scattering vectors can be seen and coincide with the hole-pocket-absent Fermi-surface topology in (B). (D,E) Topographic images of 1-UC FeSe film in different scales [D: 100×100 nm², E: 8.8×8.8 nm²; set point: (D) $V = 0.6$ V, $I = 500$ pA, (E) $V = 0.1$ V, $I = 500$ pA]. (F) Comparison between tunneling spectrum (upper panel) and angle-resolved photoemission spectra (lower panel) (23) of 1-UC FeSe. The positions of δ_1 and δ_2 are marked in (B). a.u.: arb. units. (G) Spatially resolved tunneling spectra along a 9.4-nm trajectory. The spectra have been normalized by the polynomial background extracted by a cubic-polynomial fitting for bias $|V| \geq 30$ mV. (F,G) Set point: $V = 0.04$ V, $I = 2500$ pA; modulation: $V_{\text{mod}} = 1$ mV.

The Fe atoms were deposited on 1-UC FeSe surface at ~ 143 – 155 K at an ultralow coverage (22) for the formation of individual adatoms (Fig. 2A). Spectroscopically, the adsorbate–substrate–interaction–modulated ZEBS [part I of (22)] is induced by Fe adatom (Fig. 2B), which appears as a zero-bias conductance peak (ZBCP) and is exceptionally sharp with a peak-to-dip dI/dV ratio of ~ 3 . In theory, the impurity-induced ZEBS is mostly unexpected in fully gapped superconductivity (24). Also note that, on ~ 30 -UC FeSe/SiC(0001), the Fe adatom shows no sign of the ZEBS (25). The contrast of the ZEBS that is present and absent in 1-UC FeSe/SrTiO₃ and

~ 30 -UC FeSe/SiC, respectively, implicitly signifies the necessity of topological phases predicted in the former (14, 15) for the ZEBS emergence.

To deeply reveal the physical properties of the ZEBS, the individually isolated Fe adatom (Fig. 2A) was investigated in detail (Fig. 2, C–G). The spatial evolution of the tunneling spectra departing from the Fe adatom is presented in Fig. 2C. We can see that, away from the adatom center, the zero-bias signal is abruptly suppressed but remains a single peak before being unidentified (see also Fig. S2, A and B). The unsplitting behavior of the ZEBS here is noteworthy and reminiscent of the finite-distance splitting for the MZM-like ZEBS as away from the magnetic-vortex center in the SC topological surface state (26). Meanwhile, as the ZEBS fades out towards adatom outside, the ZBCP is broadened, further evidenced by its accordingly increased full width at half maximum (FWHM) (Fig. 2D). Distinct from the IFI in $\text{Fe}_{1+x}(\text{Te},\text{Se})$ that only suppresses the phase coherence (17), the Fe adatom on 1-UC FeSe also weakens the pairing strength. Specifically, on adatom site, while Δ_2 is unaffected, Δ_1 is weakened before recovering as approaching outside (Fig. 2C). Moreover, the integrated low-bias density of states keeps roughly constant for the line spectra in Fig. 2C (Fig. S2C), meaning a spectral-weight transfer from the coherence peaks to the ZEBS. To directly visualize the ZEBS distribution in space, a dI/dV mapping for the Fe adatom in Fig. 2A was measured at 0 mV (Fig. 2, E and F). A squarish feature intimately bounded to the adatom edge was found in the ZEBS pattern, possibly due to the tunneling–matrix-element effect (27). For a more quantitative analysis, the linecut profiles starting from the adatom center were extracted from Fig. 2E and one of them (L) is exemplified in Fig. 2G. The exponential fitting of L yields a decay length ξ of 3.4 Å, which is nearly one order of magnitude smaller than the SC coherent length (2.45 nm) (28).

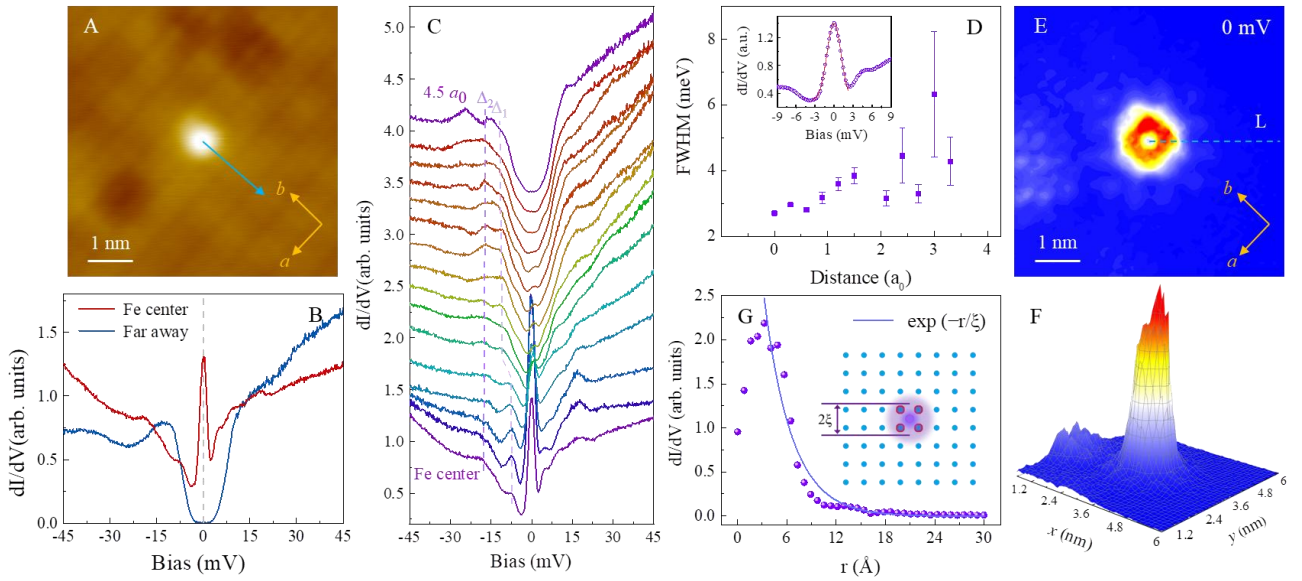


Fig. 2. Spatial evolution of the ZEBS. (A) Topographic image of an isolated Fe adatom ($6 \times 6 \text{ nm}^2$; set point: $V = 0.2 \text{ V}$, $I = 500 \text{ pA}$). (B) Tunneling spectra taken upon the Fe adatom center and far away. (C) Spatially resolved tunneling spectra (vertically offset for clarity) along the arrow in (A). The dashed lines are guides to the eyes of gap edges. a_0 : the lattice constant of surface Se lattice. (D) FWHM of the ZBCP in the tunneling spectra of (C) plotted as a function of the distance relative to the Fe adatom center. Inset: exemplifying the Gaussian fitting of the ZBCP, which defines the FWHM and error bars (standard deviations) adopted in the main panel. (E, F) dI/dV mappings at 0 mV in top and 3D views, respectively, for the Fe adatom in (A). (G) Linecut (solid symbols) along the dashed line L in (E) and corresponding exponential fitting (solid curve), showing ZBC as a function of the distance r relative to the Fe adatom center. Fitting formula: $dI/dV(r, 0 \text{ mV}) \propto \exp(-r/\xi)$; ξ : decay length. Inset: schematic of the spatial distribution of Fe-adatom scattering. (B, C, E, F) Set point: $V = 0.04 \text{ V}$, $I = 2500 \text{ pA}$; modulation: $V_{\text{mod}} = 1 \text{ mV}$.

Several candidates are available as the possible physical origins of the detected ZEBS. To be specific, Kondo impurity resonance (29), weak (anti-) localization (30) and impurity-scattering state (I) can also appear as single peaks around zero bias in the tunneling spectra. In experiments, the Kondo resonance is well described by a Fano lineshape (29) and should deviate from zero energy due to finite potential scatterings in the SC state (I). Thus, the non-Fano-like (strikingly sharp) and accurately 0-mV conductance peak here is at odds with the Kondo scenario. To put further constrains to the interpretations for the detected ZEBS, temperature-dependent experiment for the adatom-induced ZBCP was performed (Fig. 3A). As the temperature is increased, the peak intensity in the experimental spectrum is gradually decreased and completely merged at 13 K. If the ZEBS physics were dominated by the Kondo resonance or weak (anti-) localization, the ZBCP shall be irrelevant to superconductivity and persist far above T_c (30, 31), which is evidently inconsistent with the observation in Fig. 3A.

The impurity-scattering state in a superconductor may incidentally stick to the zero energy (I). Being mutually correlated, the impurity state and superconductivity should be synchronously smeared by thermal broadening (32). The temperature dependence of the ZBCP with assumed impurity-state origin is obtained by convoluting the 4.2-K spectrum taken upon the Fe adatom by Fermi-Dirac distribution function (Fig. 3A). Apparently, the zero-bias conductances (ZBCs) as a function of temperature for the experimental and convoluted ZEBS spectra remarkably diverge (Fig. 3B), meaning that the impurity-state explanation for the ZEBS is incompatible. Especially, in previous experiments, the zero-energy impurity states were mainly observed in d -wave superconductors in strong-scattering (unitary) limit (I). Besides the non- d -wave [e.g., “extended” s_{\pm} -wave (33)] pairing possibility of the 1-UC FeSe/SrTiO₃(001), the scatterings from the Fe adatoms inducing the ZEBSs here is not at the unitary limit in statistics [part I of (22)]. Furthermore, it has been theoretically predicted that the quantum-mechanically coupled adatom dimer will hybridize and split the degenerate impurity state into bonding and antibonding counterparts (34). Nevertheless, the ZEBS remains a single peak at zero energy for two closely located Fe adatoms in our case (Fig. 3, D and E). More exceptionally, compared with the ZEBS for an individual Fe adatom, the ZEBS peaks for the Fe dimer are barely suppressed in intensity. All these results for the detected ZEBS seem hardly to be reconciled within the impurity-state framework. Since the zero-energy impurity-scattering state yields no spin polarization (35), the complete exclusion of this state for the ZEBS may require the spin-resolved technique.

Previous theoretical work has shown that a TSC phase can emerge in 1-UC FeSe/SrTiO₃ (15). It has also been pointed out that magnetic impurities with critical concentration of 0.4% doped in 2D superconductors will drive a topological phase transition (36), which is more experimentally relevant to our system [$\sim 0.2\%$ – 0.3% Fe adatoms/1-UC FeSe, part I of (22)]. Thus, the inconsistency of the ZBCP with aforementioned nontopological interpretations probably suggests a topologically nontrivial scenario for the ZEBS. Phenomenologically, the ZBCP-disappearing temperature (T_c^{ZBCP}) in nearly all literatures reporting MZM-like signatures (8, 9, 18, 37) is far below the T_c of the pristine SC components in the MZM configurations. It is obvious that this empirical relation $T_c^{\text{ZBCP}} \ll T_c$ (~ 13 K \ll ~ 40 – 109 K) is well satisfied in the present situation, possibly signaling the Majorana physics involved in the Fe-adatom-induced ZEBS. By comparing with the impurity-state-like convoluted spectra in Fig. 3A where the ZBCP persists to ≥ 35 K, we found that the disappearance of the experimental ZBCP at 13 K is not a simple consequence of the thermal broadening. Additional T_c^{ZBCP} -suppression mechanism should exist, which is presumably related to the Majorana “poisoning” by thermally excited quasiparticles (38) further considering the potential TSC phase in 1-UC FeSe (15). Theoretically, the FWHM of the MZM peak in the tunneling spectrum is determined by tunneling and thermal broadening (39). To quantitatively test the MZM explanation for the ZEBS, the FWHM of the ZBCP in the experimental and convoluted spectra at various temperatures (Fig. 3A) was extracted and shown in Fig. 3C. The spectrum broadening ΔE combining both tunneling and thermal effects is also plotted for comparison. It is seen that the ZBCP FWHM is limited by ΔE for the experimental ZEBS spectra, but exceeds ΔE for the convoluted ZEBS spectra ≥ 13 K attributed to extra

dissipative broadening (39). Taken all together, the experimentally detected ZEBS in Fe adatom on 1-UC FeSe partially resembles the spectroscopic signatures of the MZM in phenomenology.

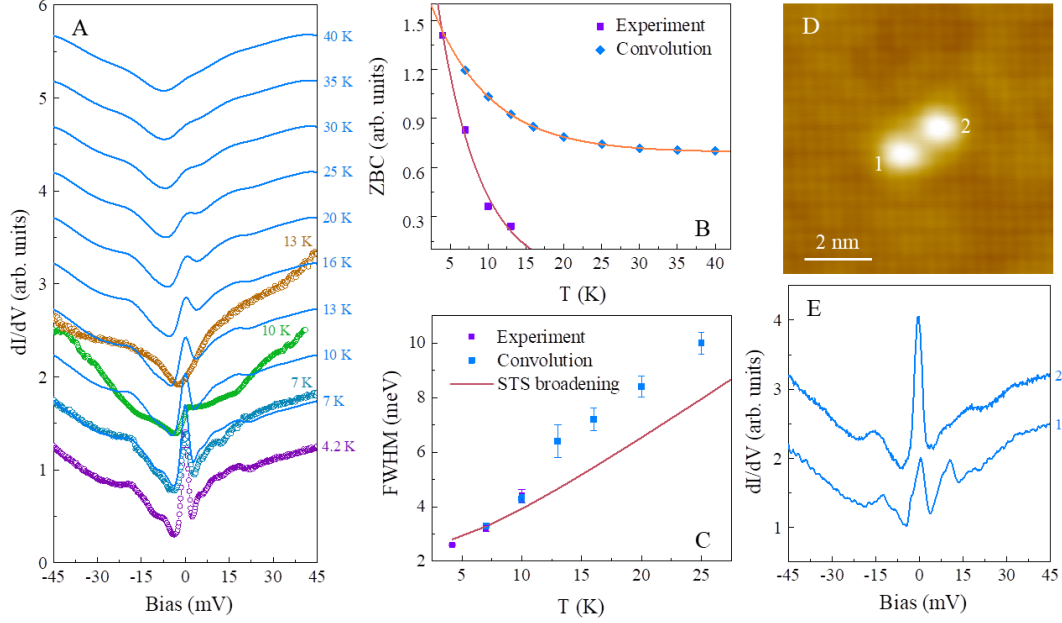


Fig. 3. Perturbation of the ZEBS by temperature and a neighboring Fe adatom. (A) Temperature dependence of the experimental tunneling spectra (open symbols) measured upon the Fe adatom center in Fig. 2A. The solid curves are convoluted 4.2-K spectrum by Fermi-Dirac distribution function. Both the experimental and convoluted spectra have been vertically offset for clarity. (B) ZBC plotted as a function of temperature (solid symbols) extracted from (A). The solid curves are tentative exponential fittings as guides to the eyes. (C) FWHM of the ZBCP (solid symbols) in the experimental and convoluted spectra of (A), which, together with the error bars, were extracted as Fig. 2(D). The solid curve is the spectral energy resolution ΔE combining both tunneling and thermal broadening, $\Delta E = \sqrt{(2.5V_{\text{mod}})^2 + (3.5k_{\text{B}}T)^2}$ (k_{B} : Boltzmann constant). STS: scanning tunneling spectrum. (D) Topographic image of an Fe-adatom dimer ($8 \times 8 \text{ nm}^2$; set point: $V = 0.1 \text{ V}$, $I = 500 \text{ pA}$). (E) Tunneling spectra (vertically offset for clarity) taken upon the Fe adatoms as numbered in (D). (A,E) Set point: $V = 0.04 \text{ V}$, $I = 2500 \text{ pA}$; modulation: $V_{\text{mod}} = 1 \text{ mV}$.

The insufficiency of the individual-YSR-atom-based MZM proposals in ideal 2D high-temperature superconductors prompts us to consider the physical pictures for the ZEBS emergence here. 1) With a sizeable magnetic moment, the Fe adatom on 1-UC FeSe modifies the local electronic structure and could further alter the local magnetic ordering. Specifically modulated short-range spin pattern may trigger the ZEBS in Fe adatom. For example, the magnetic skyrmion in proximity to a BCS superconductor can host the MZM-like ZEBS in the core (40). 2) Magnetic vortices have been suggested to be spontaneously generated in specific situations (41), part of which may be pinned under the Fe adatoms. Provided the spin-triplet pairing component owing to the spin-orbit coupling (SOC) in 1-UC FeSe, the Fe adatom located above the pinned magnetic vortex may show the ZEBS (7). 3) The odd-frequency pairing state can support the ZEBS under certain conditions (42). However, the iron-chalcogenide-based odd-frequency pairing is rarely proposed. Overall, a thorough understanding of the observed ZEBS will require detailed knowledge of the interplay among the adsorbate-substrate interaction, local spin ordering, SOC and superconductivity.

The 1-UC FeSe/SrTiO₃ adsorbed by Fe adatoms specifies overwhelming advantages for studying the ZEBS. 1) The MBE technique utilized for FeSe growth guarantees the highly disorder-free sample quality. 2) Being strictly monolayer in thickness, the 1-UC FeSe is intrinsically 2D; the rigorous two-dimensionality calls a fundamentally different mechanism of potential MZM in 1-UC FeSe from that proposed for bulk Fe(Te,Se), which relies on the

topological surface states created through the out-of-plane band inversion (12, 13). 3) The comparatively large electron pockets and SC gaps at M points for 1-UC FeSe protect the ZEBS against exotic perturbations. In future applications, the experimental system described here integrates the desired ingredients for easily realizing and manipulating the MZM-like ZEBS [part III of (22)]. The highest- T_c among iron-based superconductors for 1-UC FeSe significantly increases T_c^{ZBCP} (Fig. S3); the unnecessary of external magnetic field for inducing ZEBS, ultrashort ZEBS decay length (Fig. S3) and easy scanning-tunneling-microscope manipulation of adatoms further push our experimental system towards applicable quantum-functionality electronics [part III of (22)].

The authors acknowledge Ji Feng, X. C. Xie, Xiong-Jun Liu and Qiang-Hua Wang for helpful discussions. This work is financially supported by the National Basic Research Program of China (Grant No. 2018YFA0305600 and No. 2017YFA0303302), the National Natural Science Foundation of China (Grant No. 11774008) and the Key Research Program of the Chinese Academy of Sciences (Grant No. XDPB08-2).

1. A. V. Balatsky, I. Vekhter, J.-X. Zhu, *Rev. Mod. Phys.* **78**, 373-433 (2006).
2. C. W. J. Beenakker, *Rev. Mod. Phys.* **80**, 1337-1354 (2008).
3. K. T. Law, P. A. Lee, T. K. Ng, *Phys. Rev. Lett.* **103**, 237001 (2009).
4. C. Nayak, S. H. Simon, A. Stern, M. Freedman, S. Das Sarma, *Rev. Mod. Phys.* **80**, 1083-1159 (2008).
5. R. M. Lutchyn, J. D. Sau, S. Das Sarma, *Phys. Rev. Lett.* **105**, 077001 (2010).
6. S. Nadj-Perge, I. K. Drozdov, B. A. Bernevig, A. Yazdani, *Phys. Rev. B* **88**, 020407 (2013).
7. L. Fu, C. L. Kane, *Phys. Rev. Lett.* **100**, 096407 (2008).
8. V. Mourik *et al.*, *Science* **336**, 1003-1007 (2012).
9. H. Zhang *et al.*, *Nature* **556**, 74-79 (2018).
10. S. Nadj-Perge *et al.*, *Science* **346**, 602-607 (2014).
11. H. H. Sun *et al.*, *Phys. Rev. Lett.* **116**, 257003 (2016).
12. Z. Wang *et al.*, *Phys. Rev. B* **92**, 115119 (2015).
13. X. Wu, S. Qin, Y. Liang, H. Fan, J. Hu, *Phys. Rev. B* **93**, 115129 (2016).
14. N. Hao, J. Hu, *Phys. Rev. X* **4**, 031053 (2014).
15. N. Hao, S.-Q. Shen, *Phys. Rev. B* **92**, 165104 (2015).
16. P. Zhang *et al.*, *Science* **360**, 182-186 (2018).
17. J. X. Yin *et al.*, *Nat. Phys.* **11**, 543-546 (2015).
18. D. Wang *et al.*, *arXiv:1706.06074*.
19. Q.-Y. Wang *et al.*, *Chin. Phys. Lett.* **29**, 037402 (2012).
20. W.-H. Zhang *et al.*, *Chin. Phys. Lett.* **31**, 017401 (2014).
21. Z. Wang, C. Liu, Y. Liu, J. Wang, *J. Phys.: Condens. Matter* **29**, 153001 (2017).
22. Supplementary materials.
23. Y. Zhang *et al.*, *Phys. Rev. Lett.* **117**, 117001 (2016).
24. W.-F. Tsai, Y.-Y. Zhang, C. Fang, J. Hu, *Phys. Rev. B* **80**, 064513 (2009).
25. C.-L. Song *et al.*, *Science* **332**, 1410-1413 (2011).
26. J. P. Xu *et al.*, *Phys. Rev. Lett.* **114**, 017001 (2015).
27. I. Martin, A. V. Balatsky, J. Zaanen, *Phys. Rev. Lett.* **88**, 097003 (2002).
28. Q. Fan *et al.*, *Nat. Phys.* **11**, 946-952 (2015).
29. V. Madhavan, W. Chen, T. Jamneala, M. F. Crommie, N. S. Wingreen, *Science* **280**, 567-569 (1998).
30. D. I. Pikulin, J. P. Dahlhaus, M. Wimmer, H. Schomerus, C. W. J. Beenakker, *New J. Phys.* **14**, 125011 (2012).
31. K. J. Franke, G. Schulze, J. I. Pascual, *Science* **332**, 940-944 (2011).
32. H. Shiba, *Prog. Theor. Phys.* **40**, 435-451 (1968).

33. M. Khodas, A. V. Chubukov, *Phys. Rev. Lett.* **108**, 247003 (2012).
34. M. E. Flatté, D. E. Reynolds, *Phys. Rev. B* **61**, 14810 (2000).
35. L. Cornils *et al.*, *Phys. Rev. Lett.* **119**, 197002 (2017).
36. W. Qin, D. Xiao, K. Chang, S. Q. Shen, Z. Zhang, *Sci. Rep.* **6**, 39188 (2016).
37. S. Sasaki *et al.*, *Phys. Rev. Lett.* **107**, 217001 (2011).
38. J. R. Colbert, P. A. Lee, *Phys. Rev. B* **89**, 140505 (2014).
39. F. Setiawan, C.-X. Liu, J. D. Sau, S. Das Sarma, *Phys. Rev. B* **96**, 184520 (2017).
40. G. Yang, P. Stano, J. Klinovaja, D. Loss, *Phys. Rev. B* **93**, 224505 (2016).
41. Private communications with Z. Q. Wang.
42. Y. Tanaka, M. Sato, N. Nagaosa, *J. Phys. Soc. Jpn* **81**, 011013 (2012).

Supplementary Materials

Materials and Methods

The experiments were conducted in an ultrahigh-vacuum ($\sim 2 \times 10^{-10}$ mbar) molecular-beam-epitaxy–scanning-tunneling-microscope (MBE–STM) combined system (Scienta Omicron). The 0.7%-wt Nb-doped SrTiO₃(001) was thermally boiled by 90- °C deionized water for 50 min and chemically etched by 12% HCl solution for 45 min (1). Then the SrTiO₃ was loaded into MBE chamber and pretreated by the Se-flux method (1). The one-unit-cell (1-UC) FeSe film was grown by coevaporating high-purity Fe (99.994%) and Se (99.999%) from an e-beam evaporator and a Knudsen cell, respectively, with the SrTiO₃ held at 400 °C, followed by annealing at 450 °C for 3 h. The growth rate was estimated to be ~ 0.045 UC/min. The Fe adatoms were deposited on 1-UC FeSe surface in MBE chamber nominally at ~ 143 – 155 K. After annealing and depositing procedures, the 1-UC FeSe film was transferred *in situ* to STM chamber for topography and spectroscopy imaging. A polycrystalline PtIr tip was used throughout the experiments. The topographic images were obtained in a constant-current mode. The scanning tunneling spectra (dI/dV vs. V) (STS) were acquired by using the standard lock-in technique with a bias modulation typically of 1 mV at 1.7759 kHz. Radio-frequency–noise filters were used to enhance the signal to noise ratio. Both the topography and spectroscopy were measured with a bias voltage applied to the tip at 4.2 K unless specified. All the topographic images were post-processed by the SPIP software.

Supplementary Text

I. Adsorbate–substrate–interaction–modulated zero-energy bound state

The Fe adatoms are weakly adsorbed on 1-UC FeSe film at the energetically favored hollow sites of surface Se lattice (Fig. 2A and inset of Fig. S1A). Typically, the Fe atoms were deposited with dilute coverage of ~ 0.002 – 0.003 monolayer (ML) (e.g., Fig. S1A) (1 ML is defined as the coverage at which Fe adatoms occupy all the hollow sites of surface Se lattice). In statistics, the spins of Fe adatoms are randomly oriented, which locally modulate the exchange coupling with underlying 1-UC FeSe substrate in different degrees (2). Thus, the adsorbate–substrate–interaction–dependent Fe-adatom height accordingly appears in a statistical distribution (Fig. S1C) (2). Meanwhile, the energy of the Fe-adatom–induced bound state is similarly distributed (Fig. S1B), yielding a Gaussian profile relatively aligned with adatom-height histogram (Fig. S1, B vs. C). Consequently, the adsorbate–substrate–coupling–tuned bound-state energy for Fe adatom on 1-UC FeSe film is established in statistics. Appropriate interaction between Fe adsorbate and FeSe substrate will pin the bound state at zero energy, which corresponds to a statistical Fe-adatom height of ~ 62 pm in experiment (Fig. S1C). Particularly, the yielded adatom height for the zero-energy bound state (ZEBS) is relatively large in the Fe-adatom–height histogram (Fig. S1C), suggesting comparably weak adsorbate-substrate interaction that is evidently below the strong-interaction (unitary) limit.

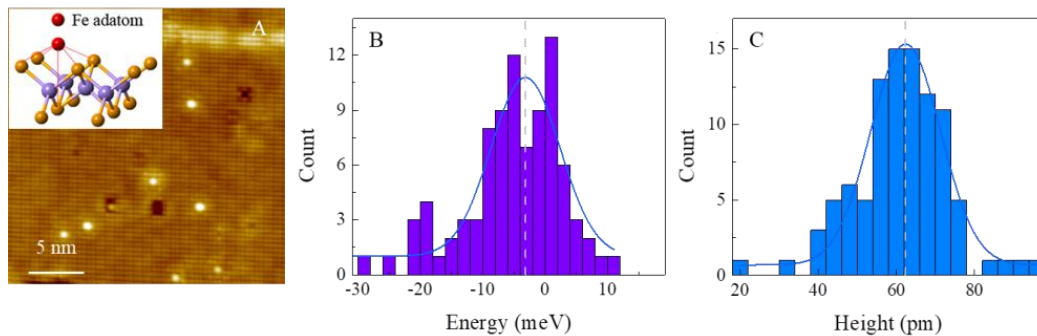


Fig. S1. Statistically correlated bound-state energy and Fe-adatom height. (A) Topographic image of Fe adatoms on 1-UC

FeSe film ($25 \times 25 \text{ nm}^2$; set point: $V = 0.2 \text{ V}$, $I = 500 \text{ pA}$). Inset: crystal structure of 1-UC FeSe with a Fe adatom centered above the hollow site of four adjacent Se atoms. (B,C) Bound-state–energy and height statistics for all measured Fe adatoms, both yielding Gaussian distributions (blue curves) with relatively aligned Gaussian-peak positions (dashed lines).

II. Additional data of the spatially evolving ZEBS

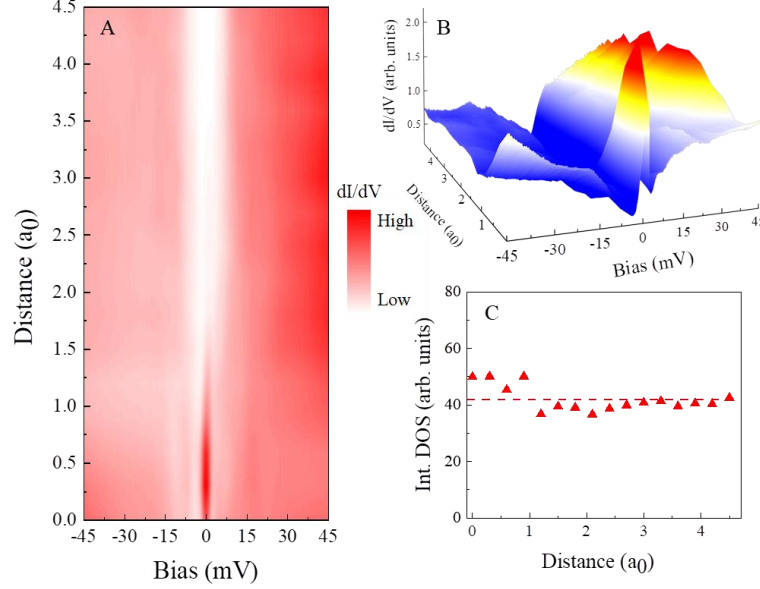


Fig. S2. More analyses of the spatially evolving ZEBS. (A,B) 2D and 3D color plots of the spatially resolved tunneling spectra in Fig. 2C. (C) Integrated density of states (DOS) (solid symbols) from -30 to 30 mV for the line spectra in Fig. 2C. The dashed line is the averaged integrated DOS as guide to the eye. The distance in (A)–(C) is defined relative to the Fe adatom center. (A,B) Set point: $V = 0.04 \text{ V}$, $I = 2500 \text{ pA}$; modulation: $V_{\text{mod}} = 1 \text{ mV}$.

III. Prospects for the local ZEBS detection in connate high-temperature superconductor

Compared with the recently prevailing systems hosting the ZEBSs, the 1-UC FeSe/SrTiO₃ integrates the desired ingredients for industrially realizing and manipulating ZEBS, which are only partially possessed by individual configurations in previous studies (Table S1; Fig. S3).

(1) *Being connate.* Artificially fabricated semiconducting nanowires (NWs) (3, 4), Fe atomic chains (5) and topological-insulator ultrathin films (6) in proximity to Bardeen-Cooper-Schrieffer (BCS) superconductors for pursuing the Majorana zero modes (MZMs) often inevitably introduce the interface unambiguity. The extrinsic complexity of configuration interface will hinder a convincing identification of the ZEBS origin. The connate 1-UC FeSe/SrTiO₃ adsorbed by Fe adatoms naturally removes the challenging interface issues.

(2) *High T_c and T_{ZBCP}* [T_c : critical temperature of the pristine superconducting (SC) components in the MZM configurations; T_{ZBCP} : existing temperature of experimentally detected zero-bias conductance peak (ZBCP)]. In previous literatures, experiments engineered the ZEBSs mainly based on proposed configurations in proximity to BCS superconductors (3-6) and on iron chalcogenide Fe(Te,Se) (7, 8). Although Fe(Te,Se) is a nominal high-temperature superconductor, its T_c is generally below 15 K (7). Therefore, in all previous MZM systems, the generic T_c involved is limited to $\sim 1\text{--}10(15) \text{ K}$. Being further “poisoned” by thermally excited quasiparticles, the MZM-like ZEBS mostly survives at $T_{\text{ZBCP}} \sim 0.05\text{--}1(4) \text{ K}$ (Table S1). As the highest- T_c [typically 65 K (9)] iron-based superconductor, 1-UC FeSe/SrTiO₃ dramatically pushes T_{ZBCP} up to 13 K .

(3) *Unnecessity of external magnetic field.* In SC-proximity-coupled semiconducting NWs and p_x+ip_y -wave

heterostructures [or Fe(Te,Se)], magnetic field B is required to trigger topological phase transition (10) and to generate magnetic vortices to bound the ZEBSs (11), respectively. The Fe adatoms on 1-UC FeSe film intrinsically induce the ZEBSs under zero external B . The unnecessary of magnetic field for inducing the ZEBS addresses promising potentials in electronics applications.

(4) *Short decay length.* The ZEBSs in Fe–atomic-chain ends and vortex centers spatially decay by several nanometers (5, 6, 8). Exceptionally, the decay length of the ZEBS induced by Fe adatoms on 1-UC FeSe film is only sub-nanometer (3.4 Å), which is also reported on interstitial iron impurity (IFI) in $\text{Fe}_{1+x}(\text{Te,Se})$ (7). Having an advantage over the IFI/ $\text{Fe}_{1+x}(\text{Te,Se})$ case, the superconductivity in 1-UC FeSe film is regained with a fully gapped and especially low-bias-DOS–depleted nature instantly away from the Fe adatom (Fig. 2, C and E; Fig. S2, A, B and D). The ultralocalized ZEBS and completely recovered SC state within short range guarantee the decoupling condition of densely deposited Fe adatoms, making the ZEBS-based high-density information processing (if any) expectable.

(5) *Being locally detected and easily manipulated.* The SC-proximity–coupled semiconducting NWs as the MZM platforms are measured by the electrical transport, yielding integrated signals (3, 4). Being capable of atomically resolved spectroscopy imaging, the STS utilized in the present experiments highlights the advantage of local ZEBS detection. For state manipulation, the intimate entanglement of the MZM-like ZEBSs at two ends of the vortex line in interfacial p_x+ip_y -wave (6) and Fe(Te,Se) (8) systems appears superfluous. In contrast, the paired-ZEBS entangling is nonexistent in the Fe-adatom situation due to the ideal two-dimensionality of 1-UC FeSe. The easy atomic-manipulation technique by using STM tip further drives the Fe-adatom/1-UC FeSe system towards applicable quantum-functionality electronics.

System	T_c/T_{ZBCP} (K)	B (T)	ξ	Local/Integrated [†]	Connate/Artificial
Au/InSb-NW/NbTiN(3)	12/0.05–0.3	≥ 0.07	—	Integrated	Artificial
Fe chain/Pb(110)(5)	7/1.4	0	~1 nm	Local	Artificial
IFI/ $\text{Fe}_{1+x}(\text{Te,Se})$ (7)	12–14/1.5–15	0	3.5 Å	Local	Connate
Point-contacted Cd_3As_2 (12)	$\leq 7.1/0.28$ –2.8	0	~ μm	Local	Artificial
Magnetic vortex/5-QL $\text{Bi}_2\text{Te}_3/\text{NbSe}_2$ (6)	7.2/0.03	+	<10 nm	Local	Artificial
Cr-Au/InSb-NW/Al(4)	1.3/0.02–0.6	>0.65	—	Integrated	Artificial
Magnetic vortex/ $\text{FeTe}_{0.55}\text{Se}_{0.45}$ (8)	14.5/0.55–4.2	+	6 nm	Local	Connate
Fe adatom/1-UC FeSe	65/4–13	0	3.4 Å	Local	Connate

Table S1. Summary of the ZEBS-related information in literatures [[†]for ZBCP-detecting technique; QL: quintuple layer; +: requiring B with unspecific strength].

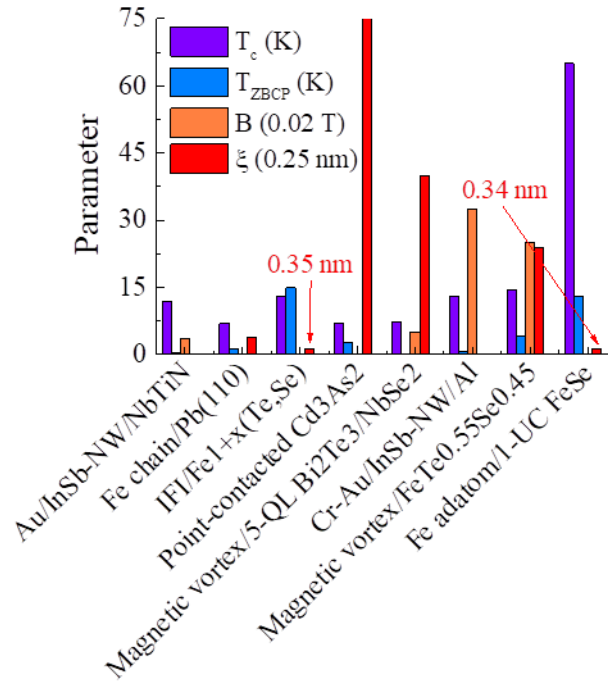


Fig. S3. Histogram of the ZEBS-related parameters in different configurations plotted for direct comparison. Magnetic field B in magnetic vortex/5-QL Bi $_2$ Te $_3$ /NbSe $_2$ and magnetic vortex/FeTe $_{0.55}$ Se $_{0.45}$ are drawn by adapting the typical values in original references (6, 8). For concrete parameter values, see Table S1.

1. Q.-Y. Wang *et al.*, *Chin. Phys. Lett.* **29**, 037402 (2012).
2. K. J. Franke, G. Schulze, J. I. Pascual, *Science* **332**, 940 (2011).
3. V. Mourik *et al.*, *Science* **336**, 1003-1007 (2012).
4. H. Zhang *et al.*, *Nature* **556**, 74-79 (2018).
5. S. Nadj-Perge *et al.*, *Science* **346**, 602-607 (2014).
6. H. H. Sun *et al.*, *Phys. Rev. Lett.* **116**, 257003 (2016).
7. J. X. Yin *et al.*, *Nat. Phys.* **11**, 543-546 (2015).
8. D. Wang *et al.*, *arXiv:1706.06074*.
9. Z. Wang, C. Liu, Y. Liu, J. Wang, *J. Phys.: Condens. Matter* **29**, 153001 (2017).
10. R. M. Lutchyn, J. D. Sau, S. Das Sarma, *Phys. Rev. Lett.* **105**, 077001 (2010).
11. L. Fu, C. L. Kane, *Phys. Rev. Lett.* **100**, 096407 (2008).
12. H. Wang *et al.*, *Nat. Mater.* **15**, 38-42 (2016).